

Supplementary Information: Strong Fermi level pinning induces high rectification ratio and negative differential resistance in hydrogen bonding bridged single cytidine pair junctions

Hao Ren,^{a*} Guangping Zhang,^b Na Lin,^c Li Deng,^a Yi Luo^{d,e} and Fang Huang^{a*}

a. State Key Laboratory of Heavy Oil Processing, Center for Bioengineering & Biotechnology, China University of Petroleum (East China), Qingdao 266580, Shandong, P. R. China.

b. School of Physics and Electronics, Shandong Normal University, Jinan, Shandong, 250014.

c. State Key Laboratory of Crystal Materials, Shandong University, 250100 Jinan, Shandong, P. R. China.

d. Hefei National Laboratory for Physical Science at the Microscale and Synergetic Innovation Center of Quantum Information & Quantum Physics, University of Science and Technology of China, Hefei, Anhui, 230026, P. R. China

e. Department of Theoretical Chemistry and Biology, School of Biotechnology, Royal Institute of Technology, S-106 91 Stockholm, Sweden.

* To whom correspondence should be addressed. Email: renh@upc.edu.cn; fhuang@upc.edu.cn.

Table of Contents

Potential energy surface

Self-consistent density functional tight binding molecular dynamics

Fermi level pinning effect for the MPSH LUMO and LUMO+1 states.

MD and electron transport for junctions with electrode distance 22.6 Å

MD and electron transport for junctions with electrode distance 23.4 Å

Electron transport properties of the charged system with electrode separation 23.0 Å

References

Potential energy surface

The potential energy surface projected along the electrode distance is obtained by optimizing the single base-pair junction with fixed electrode distances by using the Gaussian 09 package.¹ Three gold atoms were attached at each side of the base pair by bonding to the terminal sulphur atoms. These gold atoms were arranged in their in-surface configuration which is fixed during structural optimization. All the other atoms are allowed to move.

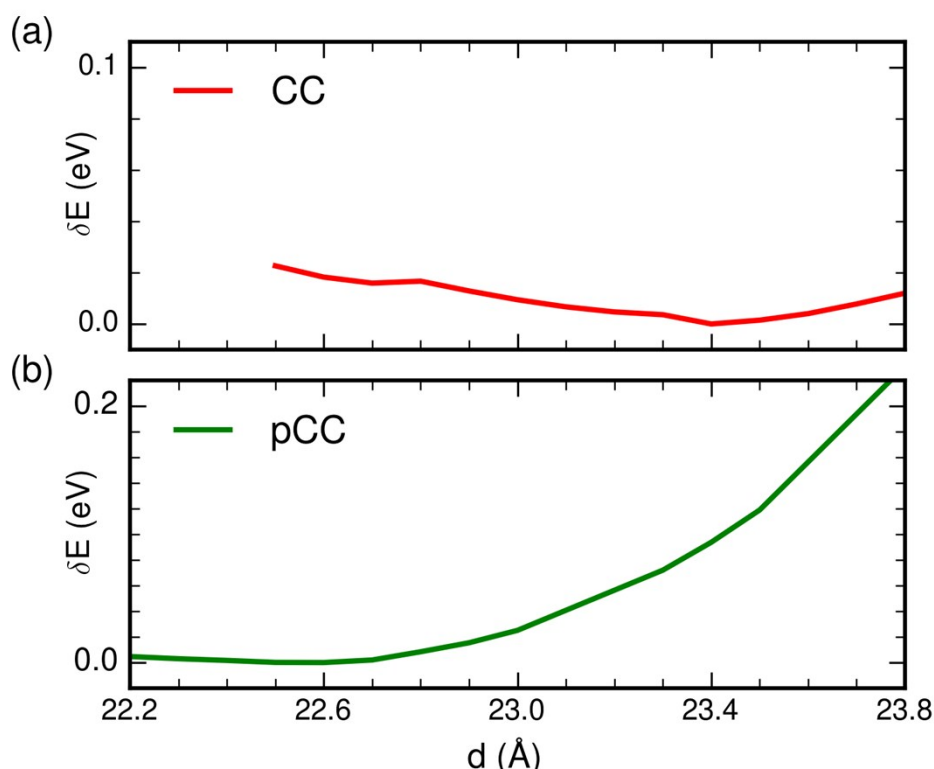


Fig. S1 Potential energies surfaces (PES) of the CC (a) and pCC (b) states projected along electrode distance.

Self-consistent density functional tight binding molecular dynamics

We examined the stabilities of the hydrogen bonds in the CC and pCC junctions with molecular dynamics simulations with semi-empirical methods at the DFTB level of theory with the DFTB+ 1.2.2 package.² The root mean squared displacements (RMSD) was calculated by only considering displacements of heavy atoms exclude hydrogen. Note that these raw RMSD values includes the

contributions from molecular translation and rotation. We used the Kabsch algorithm³ to eliminate these parts of contribution.

Fig. S2 (a) depicts the RMSD of the geometric configuration of the pCC junction respect to the energy minimized structure. It is widely accepted that a RMSD around 1.5 Å for a typical protein equilibration indicating the system is stable enough. We found that the RMSD fluctuates in the range 0.4~1.0 (0.1~1.0) Å, for pCC and CC junctions, which is sufficiently small to be considered as stable.

The evolution of the bond lengths in the hydrogen bonding framework of the junctions shown in Fig. S2 (c)-(g) also provides evidence for their stability. The red line depicts the fluctuation of the bond lengths of the covalent bond between the amino nitrogen atom in the left cytidine (N^L) and the H1 atom as labeled in Fig. 1(a). Here the superscripts attached to the atomic labels denotes atoms located in the left (L) or the right(R) region shown in Fig. 1 (a). This covalent bond is quite rigid, with a very weak fluctuation of less than 0.1 Å; on the other hand, the corresponding hydrogen bond between H1 and the keto oxygen in the right cytidine (O^R) is much flexible, with bond fluctuates around 2.0 Å with variations ± 0.2 Å. The distinct difference in the two set of bond lengths during the dynamics simulation indicates that the hydrogen bonding between the N^L, H1 and O^R atoms is asymmetric, and the barrier is sufficiently high to suppress the proton transfer from the N^L to the O^R. In Fig 3 (d) and (e), we observed the same stabilities for the hydrogen bonding sets N3L \cdots H2 - N3R and OL \cdots H3 - NR. The same data are present in Fig. 3 (f) and (g), which also witnessed the stable hydrogen bonding in the CC junction.

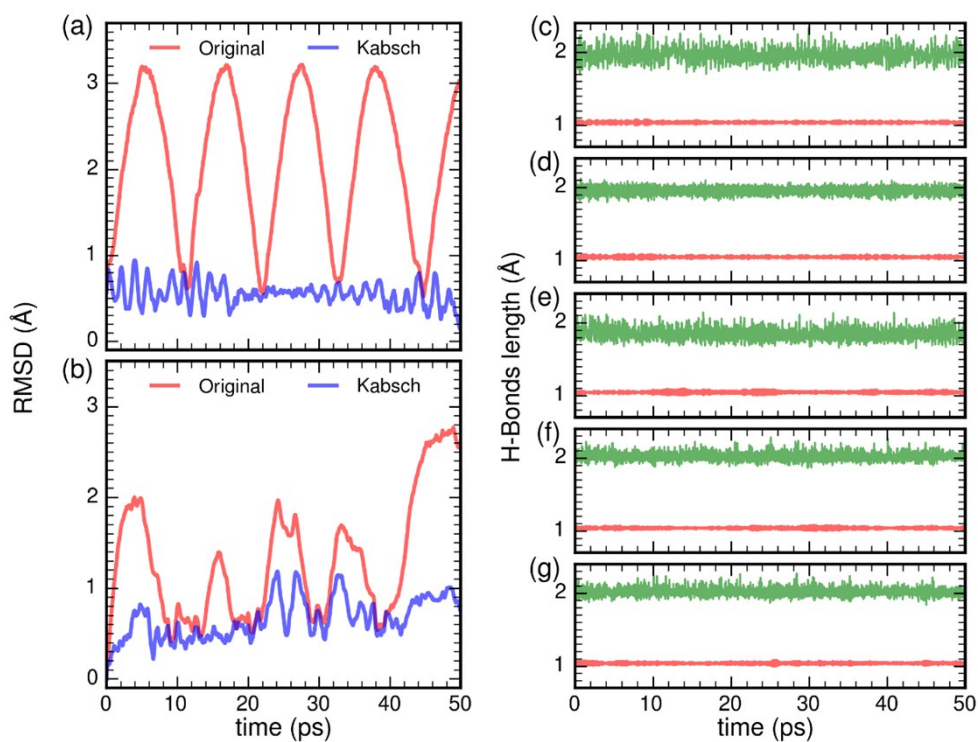


Fig. S2 Root-mean-square deviation (RMSD) of the geometric configurations of heavy atoms (exclude H) respect to the optimized structures of pCC (a) and CC (b) junctions. Red lines represent RMSD calculated from the original MD trajectories with translation/rotation contributions; blue lines represent those calculated using the Kabsch algorithm³ without translation/rotation contribution. (c) Bond length fluctuations in the pCC junction, red (blue) line denote the covalent (hydrogen) bond lengths between NL and H1L (H1L and OR). (d) and (e) Same as (c), but corresponds to bond lengths between N3L-H2R/H2R-N3R and OL-H3R/H3R-NR, respectively. (f)-(g) Same as (c), but corresponds to bond lengths between NL-H1L/H1L-N3R and N3L-H2R/H2R-NR, respectively. The numbers and superscripts attached to the atomic labels denotes atomic numbering and the left/right cytidine base illustrated in Fig. 1 (a) and (b), respectively.

Fermi level pinning effect for the MPSH LUMO and LUMO+1 states

Another interesting phenomenon is the behavior of the MPSH LUMO+1 state under bias, which sticks just above the upper bound of the energy window at positive biases, but is lifted far away from the energy window for negative biases. The gap between the MPSH LUMO and LUMO+1 increases as the bias voltage increases in the positive direction, but only slightly decreases as the bias increases in the negative direction. Since the MPSH LUMO is pinned to the left electrode Fermi level, the MPSH LUMO energy changes linearly upon applied bias, the variation trend of the LUMO—LUMO+1 gap can only be attributed to the irregular shifting of the LUMO+1 state [green dashed line in Fig. S6(b)]. This variation can be divided into three stages as the bias changes: lower than -0.3 V, -0.2~+0.2 V, and higher than +0.3 V, within each stage the energy shifts linearly with the bias. By noting that the MPSH LUMO+1 state is strongly coupled to the left electrode [see Fig. 6(f)], it is straightforward to understand that the gap opens linearly as the bias voltage increases in the forward direction, where the Fermi level pinning effects lead to downward and upward shifting for the MPSH LUMO and LUMO+1, respectively. On the other hand, at negative biases, although the MPSH LUMO+1 state is still strongly pinning to the left electrode [Fig. 6(d)], the tendency to shift down along with the left Fermi level is counteracted by the upshifting MPSH LUMO state, which is strongly pinning to the right electrode. The net effect is the contraction of the gap between the MPSH LUMO and LUMO+1 states for negative bias, as shown in Fig. S6(a).

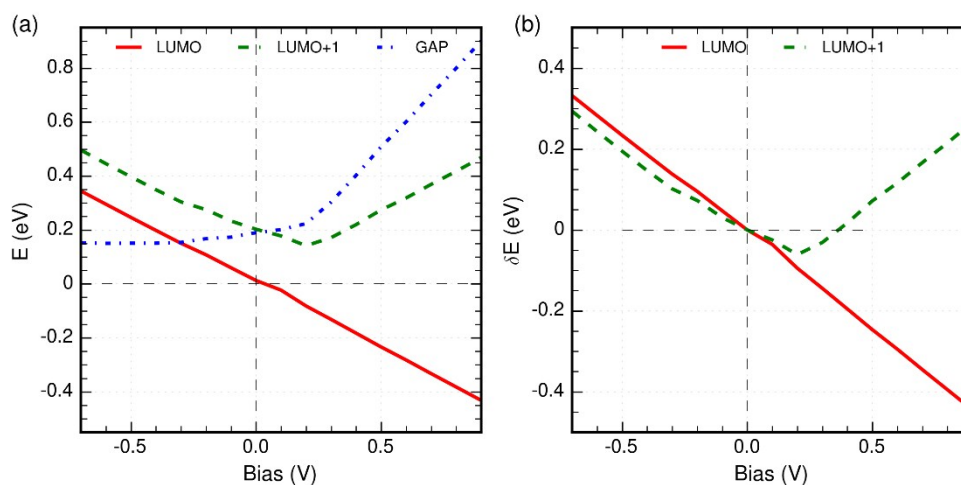


Fig. S3 (a) Illustration of the Fermi level pinning effect of the LUMO (red solid) and LUMO+1 (green dashed) MPSH eigenstates responsible for resonant transport. The gap between the two MPSH eigenstates is also present denoted by the dot-dashed line. (b) Energy shift of the LUMO (red solid) and LUMO+1 (green dashed) MPSH eigenstates under non-zero bias voltages.

MD and electron transport for junctions with electrode distances 22.6 Å

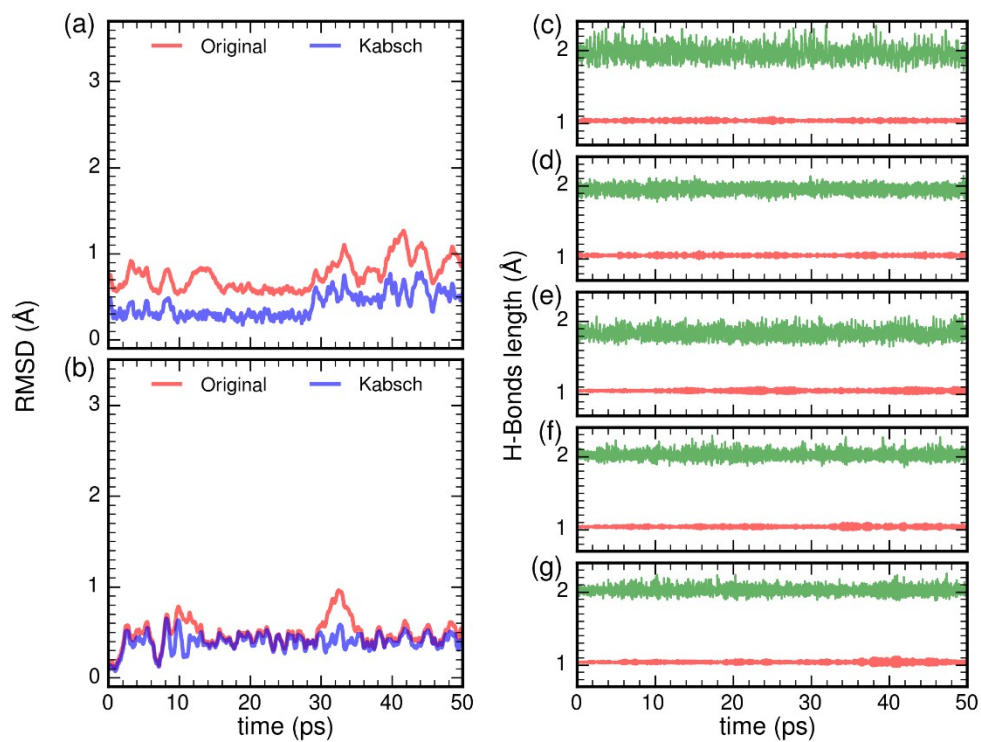


Fig. S4 The same to Fig. S2, but with electrode distance 22.6 Å.

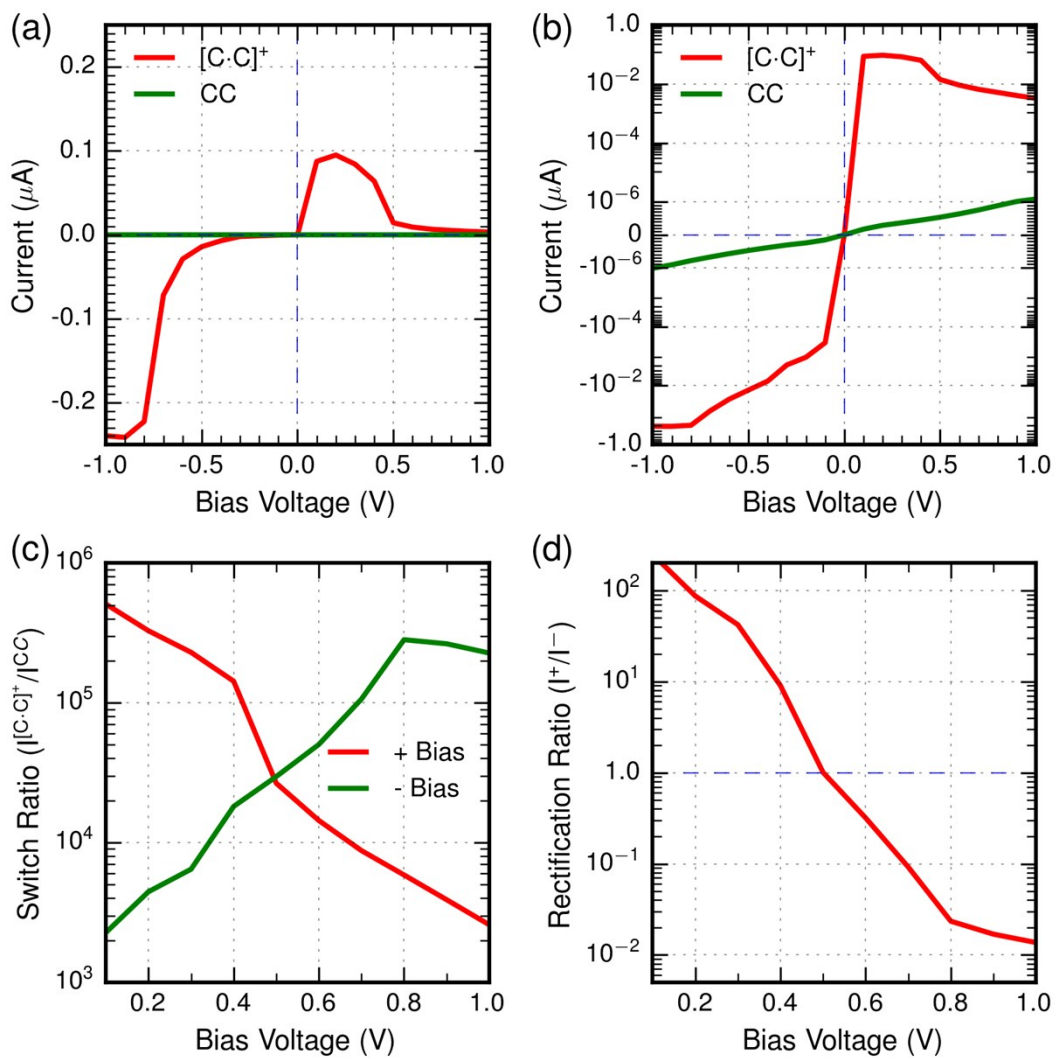


Fig. S5 The same with Fig. 3, but with electrode distance 22.6 Å.

MD and electron transport for junctions with electrode 23.4 Å

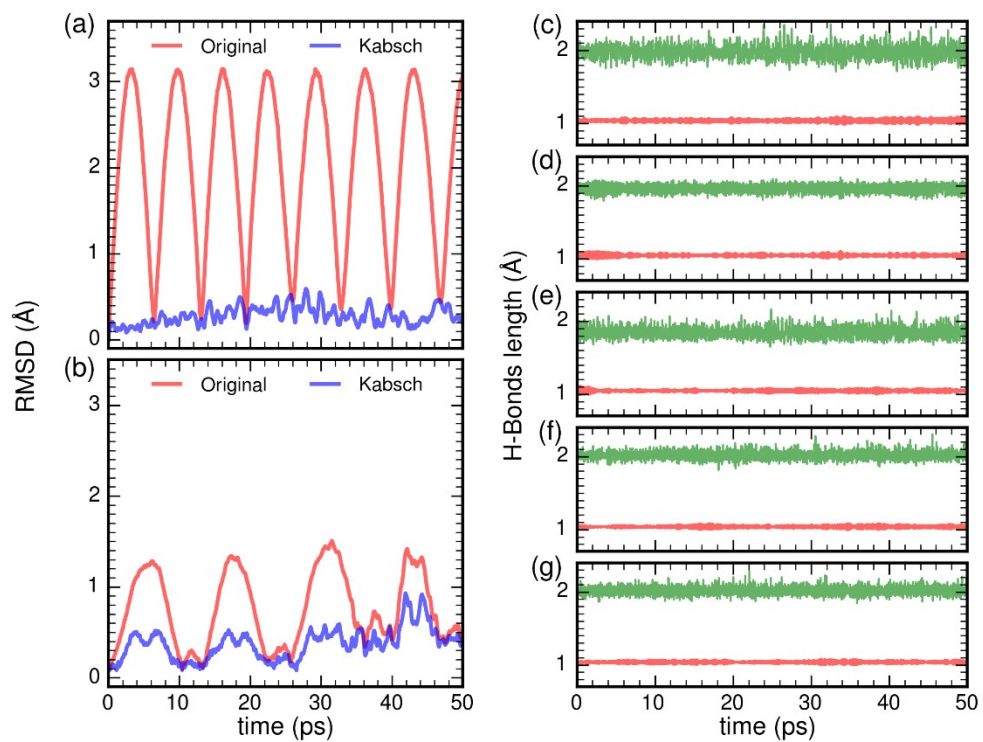


Fig. S6 The same to Fig. S2, but with electrode distance 23.4 Å.

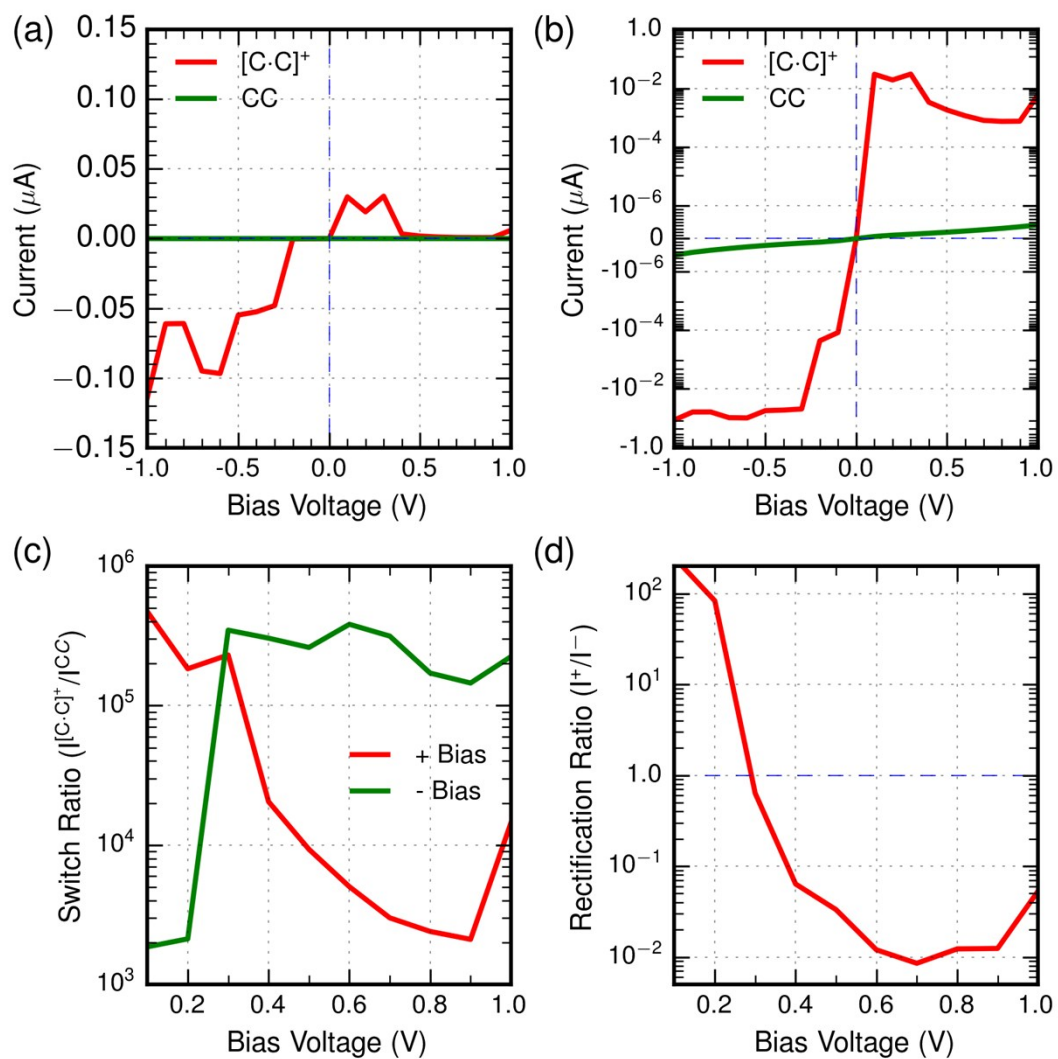


Fig. S7 The same to Fig. 3, but with electrode distance 23.4 Å.

Electron transport properties of the charged system with electrode separation 23.0 Å

The current-voltage characteristics of the charged system with electrode separation of 23.0 Å is calculated by setting the net charge of the scattering region to +1. As shown in Fig. S8, the main difference between the neutral and charged systems appears at voltages lower than -0.2 V, where the conductance of the neutral system bumps but that of the charged one remains near zero. Another difference is the conductance of the charged system is about five-fold lower than that of the neutral one. The rectifying and NDR effects also exist for the charged system. The rectification ratios at 0.1 and 0.2 V are predicted as 253 and 123, respectively, even greater than those of the neutral system.

The similar current-voltage characteristics between the neutral and charged systems stems from their similar transmission spectra, as shown in Fig. S9. Both the two systems possess two transmission channels in the integration window considered. The removal of an electron only shifts the lower transmission peak upward slightly (~ 0.01 eV). Since this channel is responsible for the electron transport at low voltages, the current response only differs slightly in the voltage range -0.2~0.2 V. The conductance of the neutral system at -0.5 V originates from the fact that the lower transmission peak gets into the integration window (Fig. S9(c), green solid line). However, for the charged system, as shown as the green dashed line in Fig. S9(c), the lower transmission peak is shifted out of the energy window, results in an insulating state.

Considering that charge should redistribute among the scattering region when connected to metallic electrodes, the neutral and charged systems discussed above would be two extreme cases. A real experimental setup would lie between these two cases. Either neutral or charged systems show similar current-voltage characteristics and similar rectifying/NDR effects at low voltage. These results support the predictions made in the manuscript, even without external gate.

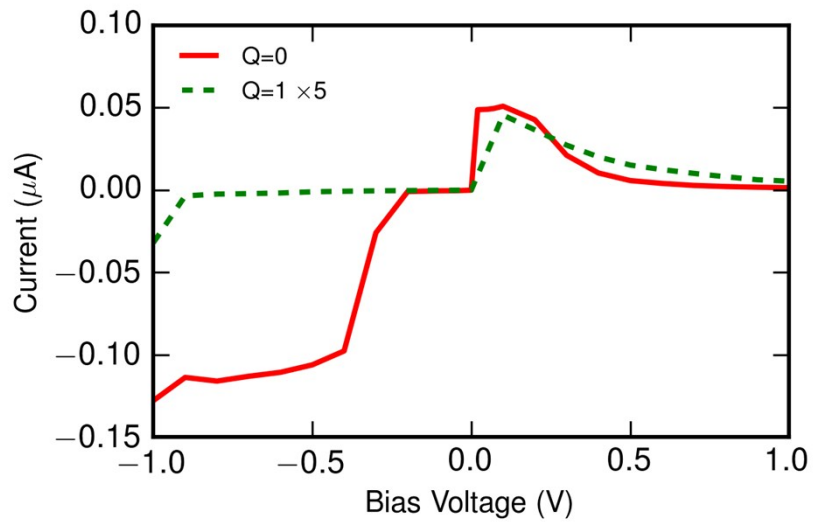


Fig. S8 Comparison between the current-voltage characteristics of the neutral ($Q=0$) and charged ($Q=1$) systems.

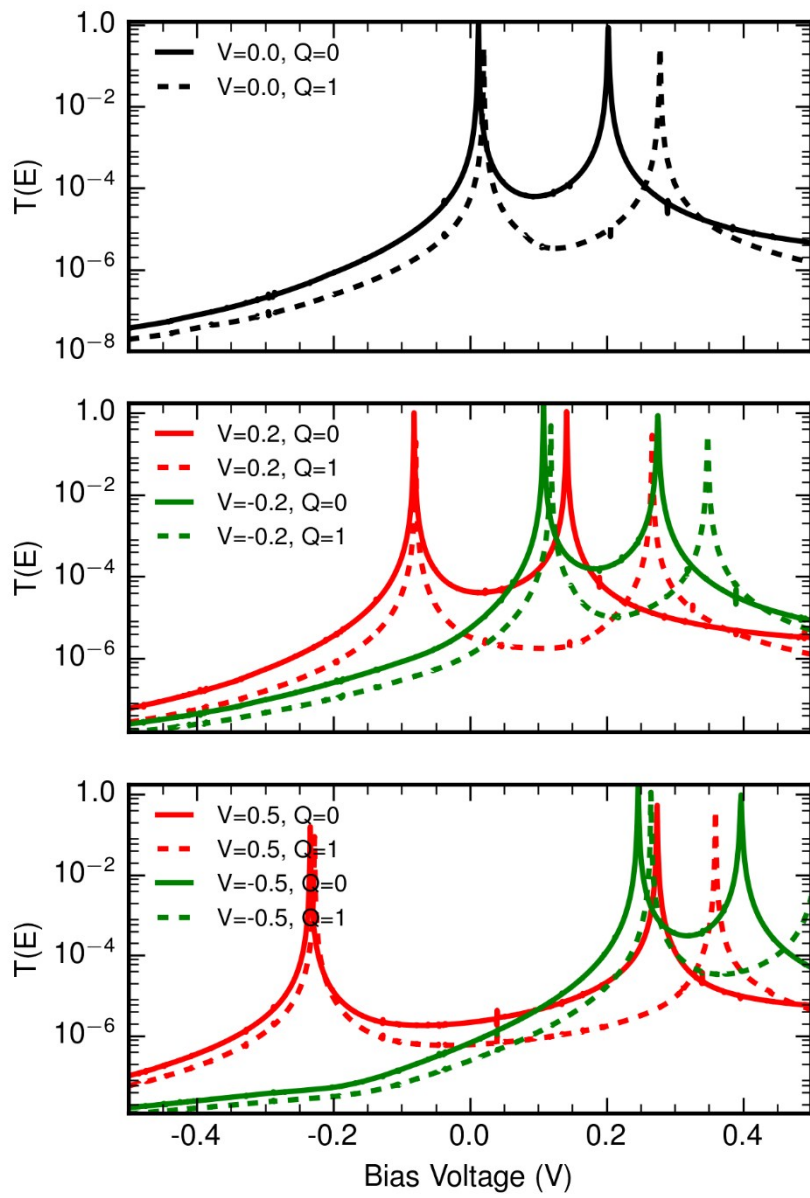


Fig. S9 Comparison between transmission functions of the neutral ($Q=0$, solid lines) and charged ($Q=1$, dashed lines) systems at bias voltages 0.0 V (a), ± 0.2 V (b) and ± 0.5 V (c), respectively.

References

- 1 M. J. Frisch, G. W. Trucks, H. B. Schlegel, G. E. Scuseria, M. A. Robb, J. R. Cheeseman, G. Scalmani, V. Barone, B. Mennucci, G. A. Petersson, H. Nakatsuji, M. Caricato, X. Li, H. P. Hratchian, A. F. Izmaylov, J. Bloino, G. Zheng, J. L. Sonnenberg, M. Hada, M. Ehara, K. Toyota, R. Fukuda, J. Hasegawa, M. Ishida, T. Nakajima, Y. Honda, O. Kitao, H. Nakai, T. Vreven, J. A. Montgomery Jr., J. E. Peralta, F. Ogliaro, M. Bearpark, J. J. Heyd, E. Brothers, K. N. Kudin, V. N. Staroverov, R. Kobayashi, J. Normand, K. Raghavachari, A. Rendell, J. C. Burant, S. S. Iyengar, J. Tomasi, M. Cossi, N. Rega, J. M. Millam, M. Klene, J. E. Knox, J. B. Cross, V. Bakken, C. Adamo, J. Jaramillo, R. Gomperts, R. E. Stratmann, O. Yazyev, A. J. Austin, R. Cammi, C. Pomelli, J. W. Ochterski, R. L. Martin, K. Morokuma, V. G. Zakrzewski, G. A. Voth, P. Salvador, J. J. Dannenberg, S. Dapprich, A. D. Daniels, Ö. Farkas, J. B. Foresman, J. V. Ortiz, J. Cioslowski and D. J. Fox, *Gaussian ~09 Revision D.01*, .
- 2 B. Aradi, B. Hourahine and T. Frauenheim, *J. Phys. Chem. A*, 2007, **111**, 5678–5684.
- 3 W. Kabsch, *Acta Cryst A*, 1978, **34**, 827–828.